PNAS RESEARCH ARTICLE | CHEMISTRY

A complete biomimetic iron-sulfur cubane redox series

Liam Grunwald[a], Martin Clémancey[b], Daniel Klose[a], Lionel Dubois[c], Serge Gambarelli[c], Gunnar Jeschke[a], Michael Wörle[a], Geneviève Blondin[b], and Victor Mougel[a,1]

Edited by Marcetta Darensbourg, Texas A&M University, College Station, TX; received December 15, 2021; accepted May 26, 2022

Synthetic iron-sulfur cubanes are models for biological cofactors, which are essential to delineate oxidation states in the more complex enzymatic systems. However, a complete series of $[Fe_4S_4]^n$ complexes spanning all redox states accessible by 1-electron transformations of the individual iron atoms (n = 0–4+) has never been prepared, deterring the methodical comparison of structure and spectroscopic signature. Here, we demonstrate that the use of a bulky arylthiolate ligand promoting the encapsulation of alkali-metal cations in the vicinity of the cubane enables the synthesis of such a series. Characterization by EPR, ^{57}Fe Mössbauer spectroscopy, UV-visible electronic absorption, variable-temperature X-ray diffraction analysis, and cyclic voltammetry reveals key trends for the geometry of the Fe_4S_4 core as well as for the Mössbauer isomer shift, which both correlate systematically with oxidation state. Furthermore, we confirm the $S = 4$ electronic ground state of the most reduced member of the series, $[Fe_4S_4]^0$, and provide electrochemical evidence that it is accessible within 0.82 V from the $[Fe_4S_4]^{2+}$ state, highlighting its relevance as a mimic of the nitrogenase iron protein cluster.

nitrogenase | iron-sulfur clusters | all-ferrous cubane | Mössbauer spectroscopy | electrochemistry

Significance

Iron-sulfur cubanes are omnipresent cofactors for electron transfer in nature and have been studied since the early 1970s. The fundamental understanding of these sites was enabled by the synthesis and characterization of small molecules with an analogous architecture as the natural $[Fe_4S_4(S^{Cys})_4]^{n-}$ site. Still, an accurate model for the most reactive so-called superreduced oxidation state was never prepared and the complete biomimetic redox series of $[Fe_4S_4]^{4+/3+/2+/1+/0}$ complexes was never traversed synthetically. In this work, we demonstrate that the use of a bulky arylthiolate ligand promoting the encapsulation of potassium cations in the vicinity of the iron-sulfur cubane allows addressing both challenges.

Iron-sulfur (FeS) clusters are ubiquitous metallocofactors, which drive the crucial biological processes to enable life on earth, ranging from iron homeostasis and gene regulation to multielectron transfer and enzymatic catalysis (1–5). Among them, cuboidal Fe_4S_4 clusters bearing cysteine ligands are the most represented structures and are found in a large number of biological systems as mediators of long-range electron transfers or directly as catalytic active sites of enzymes. This central role is a consequence of the ability of the Fe_4S_4 cluster to undergo redox changes and reversibly mediate electron transfers with low energy barriers and therefore high efficiency. In natural enzymatic systems, $[Fe_4S_4]^{0/1+/2+/3+}$ oxidation states have been observed: $[Fe_4S_4]^{1+/2+}$ is the most frequently encountered redox couple and acts reductively, the oxidative $[Fe_4S_4]^{2+/3+}$ couple is found in high-potential iron-sulfur proteins (HiPIPs), while the highly reducing $[Fe_4S_4]^0$ state has only been found in the nitrogenase iron protein (FeP). So far, there has been no evidence for the involvement of all-ferric $[Fe_4S_4]^{4+}$ clusters in biological processes (6–8).

The unambiguous identification of redox states and the in-depth understanding of the inorganic core structures in these natural systems has been directly enabled by the synthesis and study of well-defined $[Fe_4S_4(SR)_4]^{n-}$ molecular analogs (where SR refers to a thiolate ligand), whose spectroscopic signatures are key to identifying sites suggested in enzymes. However, nearly 50 y after the initial discovery of Fe_4S_4 models by Holm and among the hundreds of reported molecular Fe_4S_4 clusters, a synthetic series of all of the oxidation states accessible by 1-electron transformation of the individual Fe-atoms, $[Fe_4S_4]^{0/1+/2+/3+/4+}$, with the same ligand set has never been successfully completed. This prevents the systematic comparison of key parameters such as the core metrics of the Fe_4S_4 motif (5–7). One of the main hurdles to the preparation of such a synthetic series originates from the challenge to isolate its most reduced member; due to its extreme sensitivity toward oxidative degradation, $[Fe_4S_4(SR)_4]^{4-}$ remains the only analog of the $[Fe_4S_4(SR)_4]^{n-}$ (n = 0–4) redox series that was never synthetically isolated. This so-called superreduced all-ferrous state of the Fe_4S_4 core, $[Fe_4S_4]^0$, was first detected electrochemically in 1984 by Pickett (9) on a synthetic model of the biologically relevant $[Fe_4S_4(S^{Cys})_4]^{n-}$ site, $[Fe_4S_4(SPh)_4]^{n-}$ (10, 11), before being proposed to exist in the nitrogenase FeP (12–14). Recent studies suggested that the ability of the FeP to access the superreduced state in operando enables the enzyme to operate at twice the efficiency in terms of adenosine triphosphate (ATP) consumed per electron transferred than when operating with the $[Fe_4S_4]^{1+/2+}$ couple (2, 15). In addition, reduction to the all-ferrous state of the FeP isolated from *Methanosarcina acetivorans* was shown to catalyze the conversion of C1 substrates such as CO_2 and CO into hydrocarbons under ambient conditions (16). Finally, as a biological synthon, the superreduced FeS cubane has been proposed to play a role during the maturation of

Author contributions: V.M. conceived the study; L.G. and V.M. designed methodology and research; L.G., M.C., D.K., L.D., S.G., M.W., and G.B. performed research; L.D., S.G., G.J., G.B., and V.M. contributed new reagents/analytic tools; L.G., M.C., D.K., L.D., S.G., and G.B curated data; L.G., M.C., D.K., L.D., S.G., G.J., M.W., G.B., and V.M. analyzed data; L.G., M.C., D.K., M.W., and G.B. validated data; L.G., G.B., and V.M. wrote the paper and all authors reviewed it; L.G. and G.B. created visualizations; V.M. administered the study; and G.J., M.W., G.B., and V.M. acquired funding.

The authors declare no competing interest.

This article is a PNAS Direct Submission.

[1]To whom correspondence may be addressed. Email: mougel@inorg.chem.ethz.ch.

This article contains supporting information online at http://www.pnas.org/lookup/suppl/doi:10.1073/pnas.2122677119/-/DCSupplemental.

Published July 26, 2022.

the nitrogenase P-cluster (17, 18). However, the complexity of the enzymatic system of FeP has prevented the accurate determination of key structural and electronic parameters of the superreduced FeS core, notably *i*) the possible electronic ground states for the all-ferrous FeP, namely $S = 4$ or $S = 0$ (13, 15), *ii*) the ultraviolet-visible (UV-vis) signature for the all-ferrous state at 520 nm, which is debated as possibly originating from the Ti(III)-citrate reducing agent used to obtain the superreduced state, and *iii*) the metrics of the superreduced $[Fe_4S_4]$ core. Hence, the identification of the all-ferrous state in biological systems triggered an intense quest for well-defined physiologically relevant molecular models. In 1996, Holm and coworkers reported that the phosphine supported $[Fe_4S_4]^0$ cluster could be generated transiently in solution, but rapidly aggregates to form the more stable edge-fused all-ferrous $[Fe_8S_8]^0$ and $[Fe_{16}S_{16}]^0$ clusters over time (19). A milestone for the understanding of the geometric and electronic structure of the $[Fe_4S_4]^0$ unit has been the utilization of nonphysiological cyanide and *N*-heterocyclic carbene (NHC) ligands by Holm and Deng in 2005 and 2008, respectively, which enabled the structural characterization of the $[Fe_4S_4]^0$ core in a molecular model (20–22). The stability of the NHC-supported cubane allowed for a detailed spectroscopic characterization, revealing parameters reminiscent of biological data (13, 23). Nevertheless, NHC ligand properties differ significantly from the biologically relevant thiolate ligands; up to 15 to 30% of the metal-carbene orbital interaction energy originates from π-type metal-ligand back-bonding (24). On the contrary, thiolate ligands are stronger σ- and π-donors, creating a much weaker ligand field. This difference in binding character could alter the reactivity and spectroscopic properties of the cluster.

In this work, we demonstrate that a careful choice of bulky thiolate ligand and counter cation as well as strict exclusion of coordinating solvents enables the synthesis of a series of thiolate-supported FeS cubanes covering all oxidation states accessible within the Fe^{II}/Fe^{III} redox couples of the individual Fe atoms, ranging from all-ferric ($[Fe_4S_4]^{4+}$) to all-ferrous ($[Fe_4S_4]^0$). This permits a comprehensive analysis of the variation of the essential structural and electronic properties along the series by UV-vis absorption, electron paramagnetic resonance (EPR), ^{57}Fe Mössbauer and single-crystal X-ray diffraction (XRD) analysis.

Results and Discussion

Two rather unique features of the FeS cluster in FeP were proposed to play a role in facilitating its reduction to the superreduced state, namely its arrangement at the positive end of four α-helix dipoles and the distinct hydrogen bonding patterns surrounding the cluster (Fig. 1*A* and *SI Appendix*, Fig. S1) (2). The latter were found to be modulated upon variation of the oxidation state, adapting the environment to the cluster charge (25, 26). Interestingly, similar changes in hydrogen bonding patterns are also found for oxidized HiPIPs (27). Intending to mimic these stabilizing effects, we selected the bulky thiolate ligand $DmpS^-$ ($DmpS^-$ = 2,2″,4,4″,6,6″-hexamethyl-1,1′:3′,1″-terphenyl-2′-thiolate) as a suitable candidate because of its ability to pack redox innocent K^+ ions into the molecular assembly formed upon coordination to metal centers by cation–π interaction (Fig. 1*A*) (28, 29). Even though K^+ ions are not H-bonding donors per se, analogies can be drawn between K^+ and NH_4^+ cations regarding charge and solvation strength (30).

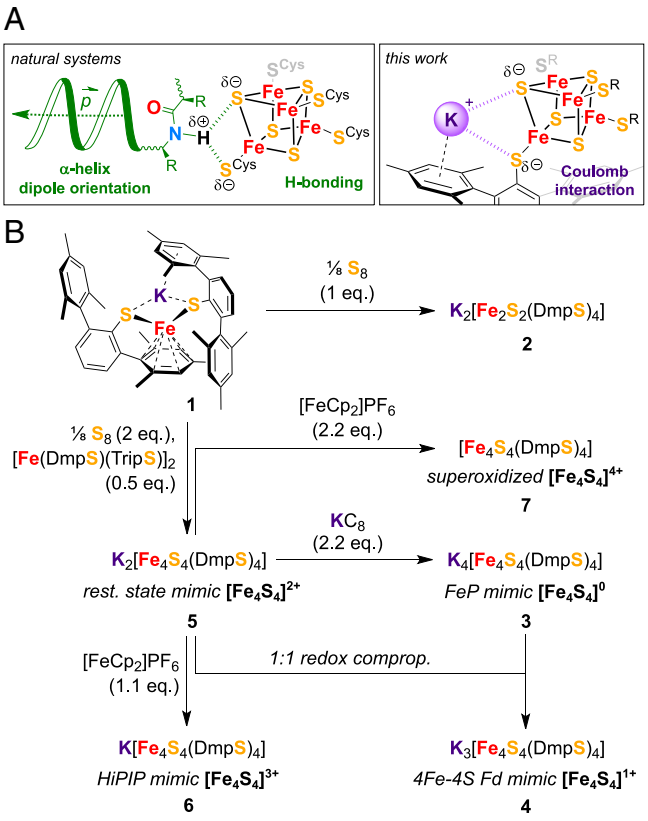

Fig. 1. Synthetic strategy used for the isolation and characterization of the redox series $K_n[Fe_4S_4(DmpS)_4]$ (n = 0–4). (*A*) Stabilization of reduced FeS cubanes in enzymes versus the strategy deployed in this work. (*B*) Schematic depiction of syntheses, whereby all reactions were carried out in toluene as solvent. Enzymatic systems and their active redox states relevant for the molecular models are indicated alongside.

A significant number of strategies for $[Fe_4S_4]^{2+}$ cluster synthesis have been reported, but most of them involve the combination of complex mixtures of sulfide sources, ligands, iron precursors, and the frequent use of other additives such as bases. As a consequence, redox-sensitive coordinating solvents able to dissociate ionic species such as acetonitrile or methanol are typically required to solubilize these precursors, yet preclude the isolation of highly reduced clusters. Thus, to perform the initial cubane assembly in redox-tolerant noncoordinating media with as few reagents as possible, we developed the synthesis of the mononuclear homoleptic Fe^I-thiolate complex $K[Fe(DmpS)_2]$ (**1**) (Fig. 1*B* and *SI Appendix*, Fig. S30). This highly reduced Fe^I precursor has the potential to act as a two-electron reductant for the generation of sulfido ligands, S^{2-}, from elemental sulfur, while being also a source of K^+ counter ions and bulky $DmpS^-$ ligands (refer to the *SI Appendix* for synthetic and characterization details). However, initial attempts to generate the $[Fe_4S_4]^{2+}$ complex upon the reaction of **1** with elemental sulfur in toluene instead resulted in the formation of the dimeric complex $K_2[Fe_2S_2(DmpS)_4]$ (**2**) (Fig. 1*B* and *SI Appendix*, Fig. S31). We reasoned that the isolation of such an Fe_2S_2 dimer resulted from the fact that the high steric hinderance of $DmpS^-$ deterred its reactivity as a reducing agent, in contrast to the typical behavior observed in traditional conditions with smaller thiolate ligands, leading to $[Fe_4S_4]^{2+}$ assemblies (31, 32). Under this assumption, we substituted 1/2 equivalent of **1** for 1/4 equivalents of $[Fe(DmpS)(TripS)]_2$ (33) in the aforementioned conditions, which allowed us to isolate the dark yellow cubane $K_2[Fe_4S_4(DmpS)_4]$ (**5**) in a 68% yield

(Fig. 1*B*). Complex **5** exhibits diamagnetic ^{1}H and ^{13}C NMR spectra accounting for all of the signals of the $DmpS^{-}$-ligand (*SI Appendix*, Figs. S13–S16). Its UV-vis absorption spectrum shows two characteristic bands at 340 and 404 nm (see Fig. 4*D*), similar to other $[Fe_4S_4]^{2+}$ cubanes supported by aromatic thiolates (10). In the solid state, **5** crystallizes 2-fold twinned in the space group $P2_12_12$ (no. 18) and contains two potassium ions, which are tightly packed around the central $[Fe_4S_4]^{2+}$ motif (Fig. 2*C*) aided by cation–π interactions from the surrounding mesityl substituents. These interactions likely play an important role in preventing the dissociation of the cation-anion pairs and maintaining **5** as a neutral molecular assembly, soluble in noncoordinating aromatic solvents.

Starting from **5**, the complete redox series could be accessed chemically (Fig. 1*B*): the all-ferrous $[Fe_4S_4]^{0}$ cluster was isolated as the dark red complex $K_4[Fe_4S_4(DmpS)_4]$ (**3**) (Fig. 2*A*) upon reduction of **5** with 2.2 equivalents of potassium graphite, while the brown singly reduced $[Fe_4S_4]^{1+}$ cluster, $K_3[Fe_4S_4(DmpS)_4]$ (**4**) (Fig. 2*B*), was prepared by comproportionation of **5** and **3**. The singly oxidized $[Fe_4S_4]^{3+}$ cluster was synthesized by the oxidation of **5** with ferrocenium hexafluorophosphate, yielding the dark purple complex $K[Fe_4S_4(DmpS)_4]$ (**6**) (Fig. 2*D*). Analogously, upon treatment of **5** with 2.2 equivalents of ferrocenium hexafluorophosphate, the all-ferric $[Fe_4S_4]^{4+}$ cluster was isolated as dark blue complex $[Fe_4S_4(DmpS)_4]$ (**7**) (Fig. 2*E*; refer to the *SI Appendix* for further details). Thus, each redox transformation is accompanied by the removal (oxidation) or the addition (reduction) of an encapsulated K^{+} ion. Such a modulation of the positive charges surrounding the cluster parallels well the varying number of H-bonding interactions of μ^3-sulfido and μ^1-thiolato ligands to the protein envelope observed with Fe_4S_4 cofactors in biological systems and found to be key to control the stability and redox potential of their different oxidation states (2, 25–27).

This analogy is supported by our electrochemical investigations. Note that in traditional electrolytes, such as $[^{n}Bu_4N][PF_6]$ in tetrahydrofuran (THF) or even in Pickett's noncoordinating eutectic system, $\{[^{n}Bu_4N][BF_4]\cdot 3$ toluene$\}$ (9), K^{+} cations are displaced due to the large excess of $^{n}Bu_4N^{+}$ cations. Therefore, as expected based on previous efforts in the field (7, 34), we were unable to traverse the complete redox series **3–7** by cyclic voltammetry in both of these electrolyte systems (*SI Appendix*, Figs. S3–S5 and refer to the *SI Appendix* for further details). To circumvent this problem, we investigated the electrochemistry of **3** and **6** in THF in the presence of a K^{+} supporting electrolyte salt, $K[BArF_{24}]$ (where $BArF_{24}$ = *tetrakis*[3,5-*bis*(trifluoromethyl)phenyl]borate). Comparing the open-circuit potentials of these two individually synthesized oxidation states of the cubane ($[Fe_4S_4]^{0}$, **3**, and $[Fe_4S_4]^{3+}$, **6**) allowed us to straightforwardly assign the redox events (see the position of the *black arrows* in Fig. 3). For direct comparison, the cyclic voltammograms of the $[Fe_4S_4]^{3+}$ cluster, **6,** recorded in THF at 100 mV s^{-1} using $[^{n}Bu_4N][PF_6]$ or $K[BArF_{24}]$ as electrolyte salts, and, correspondingly, in the absence and the presence of K^{+} ions, are combined in Fig. 3. Interestingly, while only the $[Fe_4S_4]^{2+/3+}$ and $[Fe_4S_4]^{3+/4+}$ redox couples are accessible using $[^{n}Bu_4N][PF_6]$, the complete traverse of relevant oxidation states can be observed using $K[BArF_{24}]$ within a potential window, ΔV, of a mere 1.27 V (where $\Delta V = |E_{1/2}([Fe_4S_4]^{3+/4+}) - E_{1/2}([Fe_4S_4]^{0/1+})|$; Fig. 3). Here, all redox couples appear as quasi-reversible events, as suggested by Randles-Ševčik analyses (*SI Appendix*, Fig. S6). Owing to the stabilizing effect of the K^{+} ions, the half-wave potentials of the $[Fe_4S_4]^{0/1+}$, $[Fe_4S_4]^{1+/2+}$, and $[Fe_4S_4]^{2+/3+}$ couples in the $K[BArF_{24}]$ containing electrolyte are significantly shifted anodically with respect to their counterpart in the absence of K^{+} ions (Fig. 3 and *SI Appendix*, Table S1). This appears to be particularly pronounced for the $[Fe_4S_4]^{0/1+}$ redox couple, for which the half-wave potential is only 0.19 V more cathodic than the $[Fe_4S_4]^{1+/2+}$ couple. At scan rates faster than 100 mV s^{-1}, these 2 redox waves merge into a single 2-electron reduction event, $[Fe_4S_4]^{0/2+}$ (Fig. 3 and *SI Appendix*, Fig. S7), which is in agreement with a slow electron transfer rate for the 1-electron reduction of $[Fe_4S_4]^{2+}$. We suspect this to be a consequence of the timescale of the molecular reorganization of the arylthiolate ligands, which is necessary to accommodate the packing of K^{+} ions into the assembly via the cation–π interaction, but is not significantly altered between the $[Fe_4S_4]^{1+}$ and $[Fe_4S_4]^{0}$ species. This similarity is highlighted by the nearly identical molecular architecture of **3** and **4** (same space group and similar unit cell in the solid state; Fig. 2 *A* and *B*). Near 100 mV s^{-1}, this timescale approaches the diffusion-limited regime of the voltametric measurement, thus causing the merging of the two reduction waves. The $[Fe_4S_4]^{1+}$ state could qualify as an entatic state (35): once reached and the reorganization of arylthiolate ligands is complete, the cluster is preorganized to facilitate the subsequent reduction to $[Fe_4S_4]^{0}$. This unique observation has significant implications regarding the ATP efficiency of the FeP. In this regard, three key aspects supporting the role of FeP as a 2-electron reductant (corresponding to 1 ATP per 1 electron transferred) have been identified, namely: *i*) the FeP possesses not one, but two symmetrically arranged MgATP binding sites (25, 36), *ii*) it is proposed that the FeP undergoes the same conformational changes upon both 1- or 2-electron reduction, when the Ti(III)-citrate-reduced $[Fe_4S_4]^{0}$ or the dithionite-reduced $[Fe_4S_4]^{1+}$ state are accessed (13, 37, 38), and *iii*) the ATP/e^{-} ratio approaching unity was observed in vivo, where complex physiological components were suggested to promote conformational changes and accordingly facilitate a more efficient electron transfer mechanism (2, 39). Thus, under the assumption that the K^{+} ion packing described in this work represents a suitable mimic for H-bonding interactions in nature (Fig. 1*A*), our results advocate the possible role of FeP as a 2-electron donor to the MoFeP. More specifically, if the coordination environment of the natural cofactor fulfills similar criteria as provided by the 4 rigidly packed K^{+} ions in **3**, then the $[Fe_4S_4]^{0}$ state could be accessed with somewhat surprising ease. This is further supported by the fact that in our model system, the superreduced state, $[Fe_4S_4]^{0}$, is accessible within a physiologically pertinent potential window, ΔV, of 0.82 V (where $\Delta V = |E_{1/2}([Fe_4S_4]^{2+/3+}) - E_{1/2}([Fe_4S_4]^{0/1+})|$), as compared to the enzyme's resting oxidation state, $[Fe_4S_4]^{2+}$ (2).

Beyond these electrochemical insights, the preparation of **3–7** enables a systematic approach to delineate the essential spectroscopic signatures of FeS cubanes in varying oxidation states. These signatures could, in turn, be used to facilitate the assignment of $[Fe_4S_4]^{n+}$ oxidation states in the more complex biological environments with high certainty.

Compounds **3–7** were therefore characterized by ^{57}Fe Mössbauer spectroscopy. Spectra were recorded at 80 K on the complete series of complexes and are reproduced in Fig. 4*A*. As usually observed, two main lines are detected in the spectra of compounds **4–6**. Because they present slightly different profiles, spectra were simulated with two doublets. The nuclear parameters are listed in the *SI Appendix*, Table S2. In contrast, the spectrum of **3** presents broader lines evidencing four different sites. Simulations revealed that the isomer shift values, δ, for the four sites and the quadrupole splitting values, ΔE_Q, vary in a large domain (δ from 0.57 to 0.71 mm s^{-1} and ΔE_Q from 0.82 to 2.88 mm s^{-1}). In all-ferric **7**, the four iron sites cannot be differentiated. Its nuclear parameters are similar to those

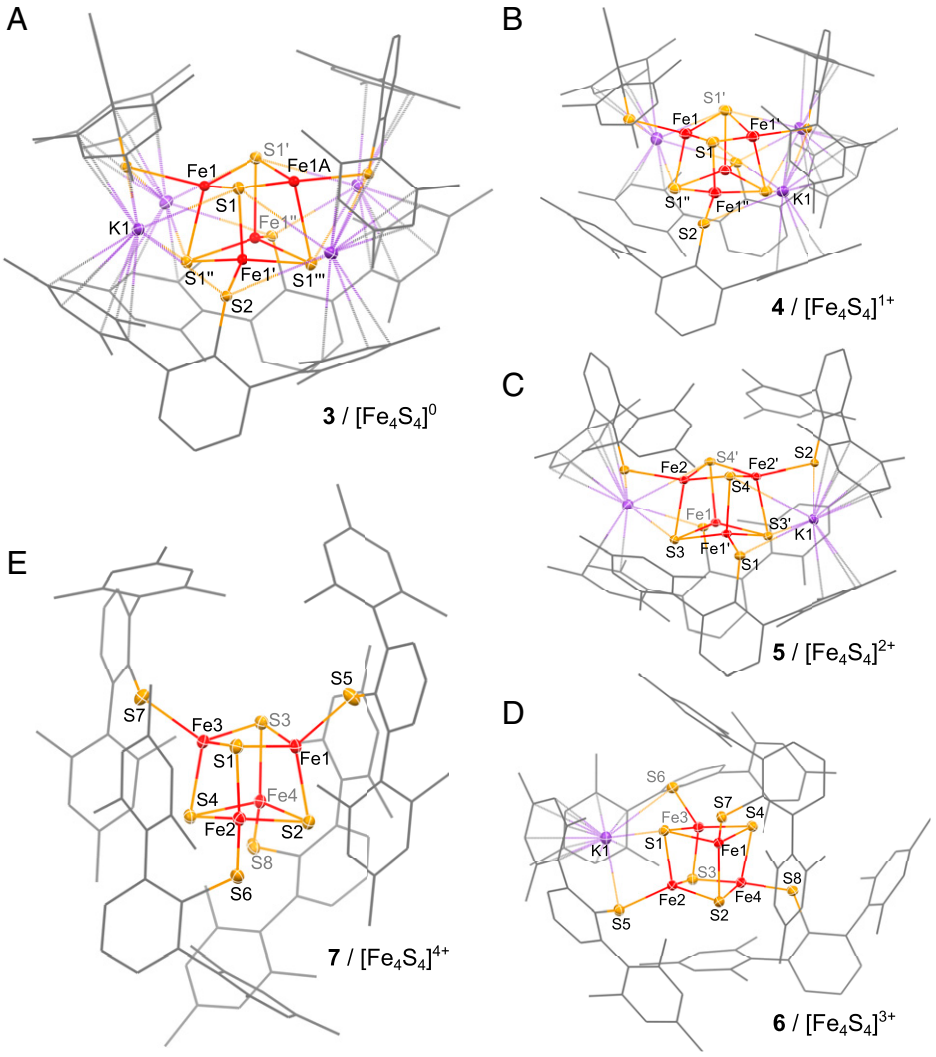

Fig. 2. Solid-state molecular structures of **3** (*A*), **4** (*B*), **5** (*C*), **6** (*D*), and **7** (*E*) in crystals of $K_4[Fe_4S_4(DmpS)_4]\cdot 2HMDSO$, $K_3[Fe_4S_4(DmpS)_4]\cdot 2HMDSO$, $K_2[Fe_4S_4(DmpS)_4]\cdot 2HMDSO$, $K[Fe_4S_4(DmpS)_4]\cdot C_7H_8$, and $[Fe_4S_4(DmpS)_4]\cdot HMDSO$, respectively. Cocrystallized solvent molecules as well as hydrogen atoms were omitted for clarity. Thermal ellipsoids at the 50% probability level are shown only for the Fe, S, and K atoms. Detailed structural parameters of **3–7** are summarized in *SI Appendix*, Tables S4–S9 and S11.

reported by Tatsumi and coworkers for the only other all-ferric cubane reported in the literature (8): $\delta = 0.32$ mm s^{-1} (here, versus 0.33 mm s^{-1} in $[Fe_4S_4(STbt)_4]$) and $\Delta E_Q = 1.03$ mm s^{-1} (here, versus 1.00 mm s^{-1} in $[Fe_4S_4(STbt)_4]$). As for $[Fe_4S_4(STbt)_4]$ (8), **7** presents an $S = 0$ ground state, which was evidenced by the 5.3-K Mössbauer spectrum recorded using a 7-T magnetic field applied parallel to the γ-beam (*SI Appendix*, Fig. S28). A comparison of the 80-K spectra clearly shows a decrease of the velocity corresponding to the central position of the absorption upon increase of the oxidation state of the complexes. Values from the *SI Appendix*, Table S2, are compiled in Fig. 4*C*. The four points are indeed aligned, and a linear fit indicates a loss of 0.075 ± 0.015 mm s^{-1} for the isomer shift per additional ferric ion.

In addition, paramagnetic compounds **3**, **4,** and **6** were analyzed by perpendicular-mode EPR spectroscopy. A frozen toluene solution of **4** exhibits an EPR spectrum consisting of two components with $S = 3/2$ and $S = 1/2$, presenting g values of (3.05, 2.64, 2.16) and (1.91, 1.98, 2.12), respectively (Fig. 4*B*; *SI Appendix*, Fig. S24*A*), and possessing nearly equal weights both at 6 K and at 10 K. This suggests that both spin states are possible ground states here, as previously reported for synthetic and natural $[Fe_4S_4]^{1+}$ systems (40, 41). The $S = 3/2$ component appears to be stronger populated in the solid state, as is evident from the spectra shown in the *SI Appendix*, Fig. S24*C*, where the $S = 1/2$ contribution disappears entirely upon immobilization of powdered **4** in eicosane. Comparatively, the X-band perpendicular mode EPR spectrum of **3** exhibits broad transitions at low field and significantly differs from the $S = 3/2$ spectrum. Similar to what had been observed for the $S = 4$ ground state with biological Ti(III)-citrate-reduced all-ferrous FeS clusters (13, 42), the absence of transitions at approximately $g = 2$, even at temperatures down to 5 K (*SI Appendix*, Fig. S23) underlines the integer-spin nature and, thus, all-ferrous oxidation state of **3**. The $[Fe_4S_4]^{3+}$ cubane, **6**, shows a rhombic EPR spectrum with principal g values of (2.072, 2.042, 2.011) and a visible g-anisotropy, which is likewise in line with the $S = 1/2$ electronic ground state found in biology as well as for previous molecular models (Fig. 4*B*; *SI Appendix*, Fig. S25) (34, 43–45).

Upon sequential 1-electron reduction, the UV-vis absorption spectra of **3–7** exhibit a decrease in intensity over most of the visible region, sharing an isosbestic point at approximately 350 nm (Fig. 4*D*). In the superreduced state, the otherwise featureless spectrum of **3** shows a pronounced shoulder at 520 nm. The origin of this band, which is also observed in the Ti(III)-citrate-reduced all-ferrous FeP, had been a topic of

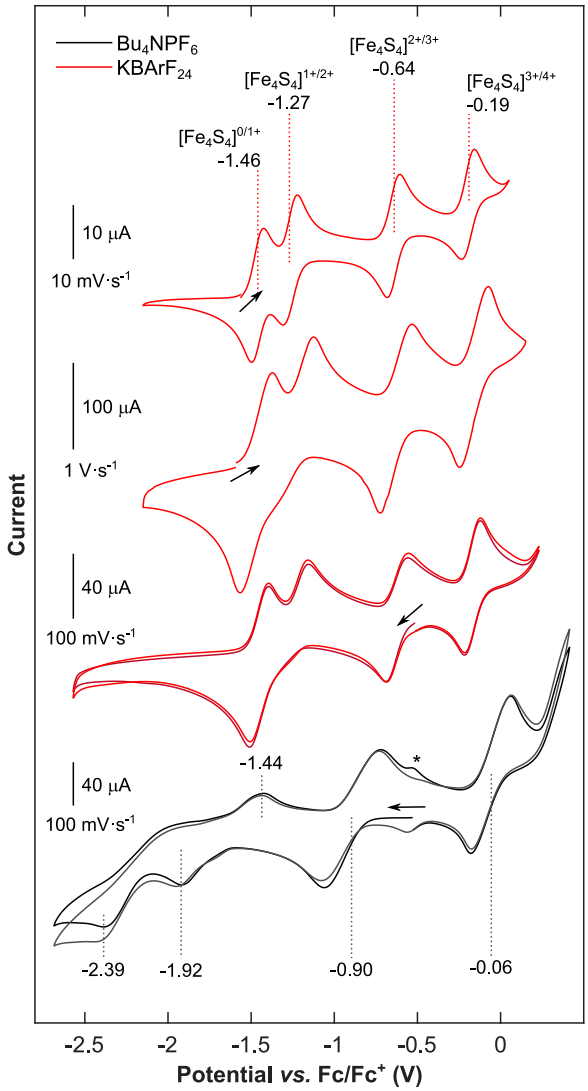

Fig. 3. Electrochemical traverse of the $[Fe_4S_4]^{0/1+/2+/3+/4+}$ redox series. (*Top Two Traces*) Cyclic voltammograms of **4** recorded in 5 mM THF solution containing 0.3 M $K[BArF_{24}]$ recorded with scan rates of 10 mV s^{-1} and 1 V s^{-1}, respectively. The first scan is shown. (*Bottom Two Traces*) Cyclic voltammograms of **6** recorded with a scan rate of 100 mV s^{-1} in 6 mM THF solution containing 0.3 M $K[BArF_{24}]$ (red lines) and in 7 mM THF solution containing 0.3 M $[^nBu_4N][PF_6]$ (gray lines), respectively, as electrolyte. Dotted lines indicate the half-wave potentials and peak potentials of individual redox events. Two subsequent scans are shown in shades of red and gray, respectively. The signal marked by an asterisk only appears after scanning at oxidative potentials and marks the reductive dissociation of $DmpS^-$ ligand from **7**, as reported elsewhere (51).

intense discussion, being attributed either to the all-ferrous FeS cluster or to the Ti(III)-citrate-reducing agent (14). The unambiguous observation of this band in the UV-vis spectrum of **3** demonstrates that it constitutes a spectroscopic signature of the all-ferrous $[Fe_4S_4]^0$ core itself. Moreover, this band had been suggested to relate to the $S = 4$ spin state of the superreduced FeS core because it was not observed in the putative all-ferrous $S = 0$ version of the FeP obtained by reduction with flavodoxin hydroquinone (15). This is in line with the spin state assignment for **3** proposed here and described below.

Besides the spectroscopic signatures, the solid-state molecular structures of compounds **3–7**, bearing the same thiolate ligand (Fig. 2*A–E*), enable a systematic comparison of the metrics of the core of the FeS cubane. To this end, structural parameters are summarized in *SI Appendix*, Table S11. Within the redox series **3–6**, the Fe_4 core volume shows a decrease as the cubane is reduced (–0.08[1] $Å^3$ per electron), in agreement with a stronger coulomb repulsion between the S^{2-} ligands and the reduced Fe centers. Concomitantly, the S_4 core volume rises (+0.33[4] $Å^3$ per electron), as shown in Fig. 4*C*. Because the increase in the S_4-volume supersedes the decrease in the Fe_4-volume, the total volume of the cubane as well as its surface area increase upon reduction, confirming the hypotheses of biological studies (2, 26, 36). The Fe–SR distances increase upon reduction (*SI Appendix*, Table S11), in agreement with the redshift of the corresponding vibration at 374–390 cm^{-1} (46) in the resonance Raman spectra of **3–7** (*SI Appendix*, Fig. S12). In a direct juxtaposition, the $[Fe_4S_4]^{0/3+}$ cores of **3** and **6**, respectively, exhibit low root-mean-square distances compared to structure data collected on the corresponding cofactors in their active redox state (root-mean-square deviation [RMSD](**3**/1G1M) = 0.074 and RMSD(**6**/1HPI) = 0.048; see *SI Appendix*, Fig. S43). Note that aside from the structural distortion of the FeS core and the packing of K^+ ions, the overall connectivity and architecture of clusters **3–7** is invariant across all five oxidation states, exemplifying the ability of FeS cubanes to mediate multielectron processes with marginal reorganization (Fig. 2). The all-ferric cluster **7** identifies as somewhat of an outlier, exhibiting a smaller S_4 core volume, yet also a smaller Fe_4 core volume compared to its 1-electron reduced analog, **6**. This has been observed previously and can be attributed to differences in the internal magnetic coupling scheme as well as the smaller ionic radius of Fe^{III} compared to Fe^{II} (8). Overall, the data presented here provide a quantitative scale for systematic geometric changes occurring in the Fe_4S_4 core upon variation of the oxidation state, which could facilitate redox assignments in the more complex enzymatic environments. Based on Fig. 4*C*, we propose two putative observations: *i*) The Fe_4-volume appears generally underestimated; and *ii*) a multitude of biological $[Fe_4S_4]^{2+}$ or $[Fe_4S_4]^{1+}$ sites—1HLQ or 1CP2 for example—have been reported with metrics resemblant of more reduced forms, $[Fe_4S_4]^{1+}$ or $[Fe_4S_4]^0$, respectively, advocating the fact that oxidation state assignments in protein single crystals are not unambiguous and that the role of photoreduction in the X-ray beam is perhaps underrated (47).

Based on the results from UV-vis absorption, zero-field ^{57}Fe Mössbauer and perpendicular-mode EPR spectroscopy presented above, a $S = 4$ spin ground state may be suggested for **3**. To further confirm this assignment, applied-field ^{57}Fe Mössbauer, parallel-mode EPR, SQUID magnetometry and temperature-dependent single-crystal XRD analyses were carried out. The 2.5-K and 7-T ^{57}Fe Mössbauer spectrum of **3** (Fig. 5*A*) is very similar to that of Ti(III)citrate-reduced *Azobacter vinelandii* (*Av2*), strongly advocating the $S = 4$ ground state (48). Moreover, as for *Av2*, upon subtraction of the 10-mT spectrum recorded at 2.5 K from that recorded at 5.8 K, the resulting difference can be deconvoluted in doublets, indicating a similar electronic structure. In contrast to *Av2* but in agreement with the 80-K spectrum shown above, they are four in a 1:1:1:1 ratio (*SI Appendix*, Fig. S26). The simulation was performed with eight lines presenting the same linewidth and the same area. Among the 105 possible pairings, only the one presented in *SI Appendix*, Fig. S26, gives four doublets with similar isomer shifts. The δ values lie between 0.57 and 0.69 mm s^{-1} (*SI Appendix*, Table S3), with a 0.63 mm s^{-1} average value that is close to that determined for the all-ferrous cluster of *Av2* (0.68 mm s^{-1}). The quadrupole splitting values, ΔE_Q, range from 0.81 to 3.03 mm s^{-1}, a larger domain than that of the protein (1.24–3.08 mm s^{-1}). A simulation of the 2.5-K and 7-T spectrum of **3** is proposed in Fig. 5*A* (see *SI Appendix*, Fig. S27

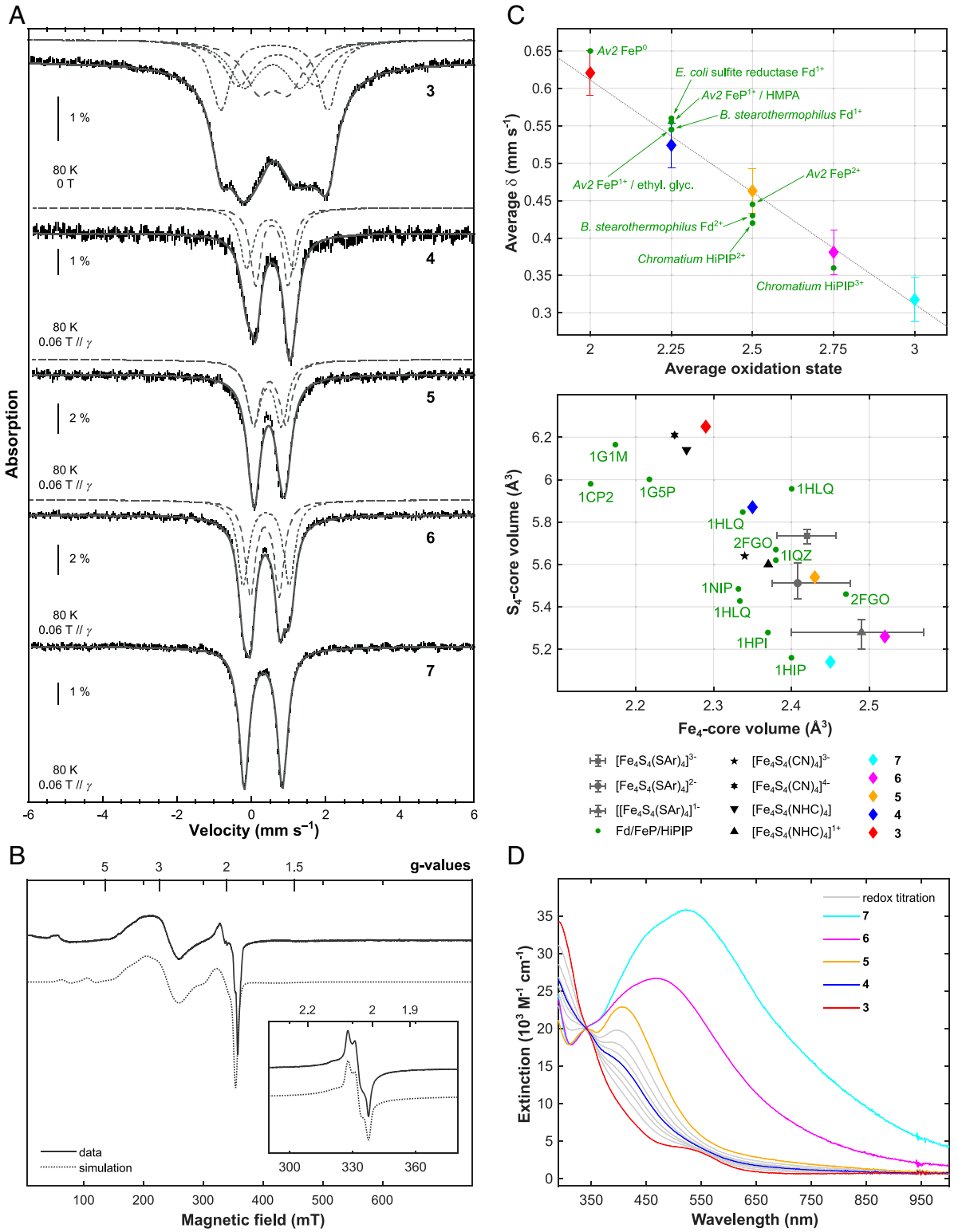

Fig. 4. ^{57}Fe Mössbauer, EPR, UV-vis electronic absorption and geometric data for clusters **3–7**. (*A*) Mössbauer spectra (hatched bars) recorded on powder samples at 80 K with a 0.06-T external magnetic field applied parallel to the γ-beam for **4–7** and at zero-field for **3**. Simulations are overlaid as gray solid lines and deconvolutions are displayed above. See *SI Appendix*, Table S2, for the parameter values. Note that for the Mössbauer spectrum of **7**, an impurity accounting for 4% of the total Fe content has been subtracted (δ = 0.96 mm s^{-1}, ΔE_Q = 2.09 mm s^{-1}, Γ_{fwhm} = 0.25 mm s^{-1}). (*B*) X-band perpendicular mode EPR spectra of 2 mM toluene solutions of **4**, recorded at 10 K and **6** (*Inset*), recorded at 40 K. Data are represented by solid lines and simulations by dotted ones. For details of the fitting parameters, refer to *SI Appendix*, Figs. S24 and S25. (*C*, *Top*) Averaged value of the isomer shift issued from the simulations of the 80-K Mössbauer spectra upon the averaged oxidation state of the iron ions in complexes **3–7**. The gray dotted line is a linear fit of the four experimental points. Data recorded on selected biological systems are shown as green dots. (*C*, *Bottom*) Variation in the Fe_4 and S_4 core volumes of selected FeS cubane containing structures of biological (FeP, 4Fe-4S Fds, and HiPIP) and synthetic origin. Synthetic models of aromatic thiolate supported cubanes span 8, 11, and 5 examples for $[Fe_4S_4(SAr)_4]^{1-}$, $[Fe_4S_4(SAr)_4]^{2-}$, and $[Fe_4S_4(SAr)_4]^{3-}$, respectively. The data are represented by a gray triangle, dot, and square in the position of the arithmetic mean. Bars indicate the maximum and minimum values reported. Data for the redox series **3–7** are shown by red, blue, yellow, magenta, and cyan diamonds with error bars; refer to *SI Appendix*, Table S12, for all values and references. (*D*) UV-vis electronic absorption spectra of 1.1 · 10^{-4} M toluene solutions of compounds **3** (red), **4** (blue), **5** (yellow), **6** (magenta), and **7** (cyan). Solid gray lines indicate spectra measured along the stoichiometric redox comproportionation reaction between **3** and **5**, which results in the formation of **4**.

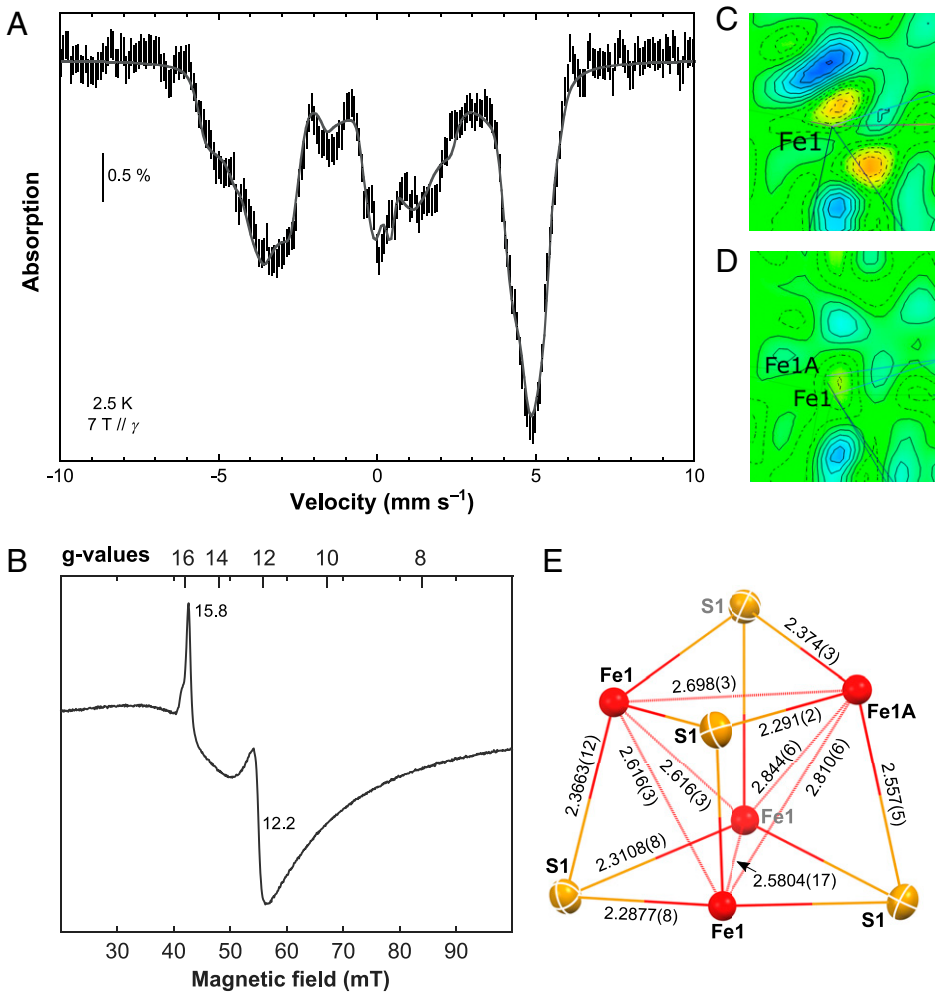

Fig. 5. Spectroscopic and structural data for **3**. (*A*) 2.5 K Mössbauer spectrum recorded on a powder sample of **3** using a 7-T external magnetic field applied parallel to the γ-beam (hatched bars). A simulation is overlaid as a gray solid line, and the corresponding list of parameters is given in *SI Appendix*, Table S3. (*B*) Low-field region of the parallel-mode EPR spectrum of a 10-mM frozen toluene/cyclohexane (9:1) solution of **3** recorded at 6 K. (*C*, *D*) Difference electron density map (–0.74 e/Å^3 (red) to 0.751 e/Å^3 (blue); iso-values in increments of 0.1147 e/Å^3) of a mean plane through the Fe1-position before (*C*) and after (*D*) applying the split model, highlighting the smoothing of the residual electron density upon refining the disorder. (*E*) Solid-state molecular structure of the Fe_4S_4 unit in **3** at 100 K, containing three symmetry equivalent iron-atoms (Fe1 site with an occupancy of 0.797(8)) and one iron atom of the Fe1A site with an occupancy of 0.203(8). The disorder described by the split model corresponds to a superposition of this locally ordered unit in four different orientations. Distances are given in angstroms.

and Table S3 for the deconvolution and the parameter set, respectively). Only site 1 presents positive hyperfine values, while sites 2–4 have negative values, in fair agreement with the spin alignment expected for a $S = 4$ ground state. The isotropic components (4.1, –8.2, –7.4, –8.0 T) are between those determined on the $[Fe_4S_4]^0$ cluster isolated with a NHC-based ligand (21) and those of *Av2*. The effective magnetic moment, μ_{eff}, presents a value of 8.48 μ_B at 2 K, which is slightly lower than the expected spin-only value of 8.94 μ_B for a nonet, and increases to 9.82 μ_B at 300 K (*SI Appendix*, Fig. S29), corroborating the $S = 4$ assignment. Furthermore, the low field region of the EPR spectrum of a frozen solution of **3** recorded in parallel mode exhibits two sharp features with *g* values of 15.8 and 12.2. This agrees with the previous studies of $[Fe_4S_4]^0$ clusters with $S = 4$ ground states, leading us to attribute these transitions to the ground state doublet ($M_s \pm 4$) and the first excited doublet ($M_s \pm 3$) of the $S = 4$ manifold, respectively (Fig. 5*B*) (13, 21, 42, 48).

Such a $S = 4$ spin state has been shown to give rise to a structural distortion of the Fe_4S_4 core, resulting in three symmetrically equivalent sites and one inequivalent site (3:1 distortion) (21). This appears at first sight to be incompatible with the single-crystal XRD data recorded on **3** at 100 K, as the proposed tetragonal space group $P\bar{4}2_1c$ (no. 114) imposes a fully symmetrical Fe_4S_4 unit with a single Fe center in the asymmetric unit. However, a close inspection of the difference Fourier map for the single-crystal XRD data (*SI Appendix*, Fig. S37) revealed that a single ellipsoid in the position of Fe1 cannot properly account for the observed electron density. Instead, a description applying a split model using two partially occupied Fe sites (Fe1 and Fe1A) proved to be superior, as highlighted by the significant smoothing of the residual electron density in the difference Fourier map surrounding the Fe1 position after applying the split model (Fig. 5*C* and *D*). The final refinement, constraining the sum of the occupancies to 1 and the isotropic displacement parameters for both split positions to be equal, converges at an occupancy ratio of 0.797(8):0.203 (8) at 100 K for Fe1 and Fe1A, respectively. This Fe1:Fe1A occupancy ratio of 80:20 is slightly higher than expected for the $S = 4$ ground state, for which a 75:25 ratio should be adopted. Therefore, the evolution of the site occupancies was determined from a series of measurements performed at varying temperatures. The extrapolation to 0 K gives an occupancy for Fe1 of almost exactly 0.75, as it is expected for a fully occupied $S = 4$ ground state

(*SI Appendix*, Fig. S40; for further details, refer to the *SI Appendix*). This is in line with the temperature dependence of the effective magnetic moment, μ_{eff}, which also shows a linear decrease with lower temperature until ~15 K (*SI Appendix*, Fig. S29). Fe1A therefore corresponds to the antiferromagnetically aligned iron site of the nonet spin state, which perturbs the tetragonal symmetry ($P\bar{4}2_1c$) of the Fe_4S_4 core due to magneto-structural correlation. This results in a domain of Fe-Fe and Fe-S distances in **3**, ranging from 2.844(6) to 2.5804 (17) Å and from 2.557(5) to 2.2877(8) Å, respectively (Fig. 5*E*), being larger than that of the NHC-based system (22) and similar to what had been suggested based on computational and spectroscopic studies of the all-ferrous FeP (*SI Appendix*, Table S13) (49, 50).

Conclusions

The solid-state structure and spectroscopic signature of superreduced all-ferrous **3** confirms the broken-symmetry $S = 4$ electronic ground state. This provides a decisive argument in long-standing debates concerning the fundamental geometric and electronic structure of the hitherto elusive $[Fe_4S_4]^0$ oxidation state encountered in natural FeS cubane cofactors. More broadly, we found that the use of thiolate ligands promoting the coordination of alkaline cations in the vicinity of the cubane via the cation–π interaction enables the synthesis of a complete redox series of biomimetic FeS cubanes and their study by cyclic voltammetry. This illustrates the relevance of using K^+ ions to mimic the stabilizing H-bonding and α-helix dipoles found in natural systems. The physiologically pertinent potential window observed here for the reduction of the $[Fe_4S_4]^{2+}$ cluster to its all-ferrous oxidation state supports the possible involvement of $[Fe_4S_4]^0$ intermediates in the electron transfer pathway between the FeP and MoFeP of nitrogenase in operando. The redox series **3–7** enabled quantitatively uncovering fundamental relationships between the oxidation state of the cubane, its Mössbauer isomer shift, and the volumetric parameters of the Fe_4S_4 core. We expect these trends to aid the assignment of oxidation states of FeS cubanes in the more complex biological environments and are currently pursuing in-depth spectroscopic and theoretical analyses of **3–7**, which should lead to a rational understanding of the variation of their electronic structure.

Materials and Methods

Unless specified otherwise, the chemical reactions described herein were carried out at room temperature under an inert argon atmosphere using Schlenk techniques or a glovebox and in dry and degassed solvents. In general, the $[Fe_4S_4]^{0/1+/2+/3+/4+}$ (**3–7**) redox transformations were straightforwardly accomplished using KC_8 as reductant and ferrocenium hexafluorophosphate as oxidant in a toluene solution. Comprehensive procedures for all of the syntheses, solvent preparation, spectroscopic sample preparation, as well as additional characterization details, including cyclic voltammetry, UV-vis absorption, ^1H and ^{13}C NMR, EPR, ^{57}Fe Mössbauer, and single-crystal XRD data, are compiled in the *SI Appendix*. The analytical purity of compounds **1–7** was established based on the physical methods discussed in this work as well as elemental analyses performed on the bulk of independently synthesized samples.

Data Availability. The solid-state molecular structures of all of the compounds discussed have been deposited as crystallographic information files in the Cambridge Structural database: 2124635 (**3**), 2124636 (**2**), 2124637 (**5**), 2124638 (**4**), 2124639 (**6**), 2124640 (**1**) and 2167405 (**7**). All other data, including details of syntheses and spectroscopic measurements, are available in the main text and/or the *SI Appendix*.

ACKNOWLEDGMENTS. J.-F. Jacquot is acknowledged for his assistance with the SQUID measurements. L.G. and V.M. thank the European Research Council (ERC) under the European Union's Horizon 2020 research and innovation program (Grant Agreement No. 853064); M.C. and G.B. thank the Labex ARCANE and CBH-EUR-GS (ANR-17-EURE-0003) for funding. L.G. thanks the Swiss Scholarship of the Chemical Industry for funding.

Author affiliations: [a]Department of Chemistry and Applied Biosciences (D-CHAB), ETH Zürich, CH-8093 Zürich, Switzerland; [b]University of Grenoble Alpes, CNRS, Commissariat à l'énergie atomique et aux énergies alternatives (CEA), Institut de Recherche Interdisciplinaire de Grenoble (IRIG), Laboratoire de Chimie et Biologie des Métaux, Physicochimie des Métaux en Biologie (PMB), CEA Grenoble, Grenoble Cedex, F-38054 France; and [c]University of Grenoble Alpes, CNRS, CEA, IRIG, Systèmes Moléculaires et nanoMatériaux pour l'Énergie et la Santé (SyMMES), CEA Grenoble, Grenoble Cedex, F-38054 France

1. B. K. Burgess, D. J. Lowe, Mechanism of molybdenum nitrogenase. *Chem. Rev.* **96**, 2983–3012 (1996).
2. H. L. Rutledge, F. A. Tezcan, Electron transfer in nitrogenase. *Chem. Rev.* **120**, 5158–5193 (2020).
3. E. O'Brien *et al.*, The [4Fe4S] cluster of human DNA primase functions as a redox switch using DNA charge transport. *Science* **355**, 1789 (2017).
4. N. Maio *et al.*, Fe-S cofactors in the SARS-CoV-2 RNA-dependent RNA polymerase are potential antiviral targets. *Science* **373**, 236–241 (2021).
5. A. E. Boncella *et al.*, The expanding utility of iron-sulfur clusters: Their functional roles in biology, synthetic small molecules, maquettes and artificial proteins, biomimetic materials, and therapeutic strategies. *Coord. Chem. Rev.* **453**, 214229 (2022).
6. P. Venkateswara Rao, R. H. Holm, Synthetic analogues of the active sites of iron-sulfur proteins. *Chem. Rev.* **104**, 527–559 (2004).
7. S. C. Lee, W. Lo, R. H. Holm, Developments in the biomimetic chemistry of cubane-type and higher nuclearity iron-sulfur clusters. *Chem. Rev.* **114**, 3579–3600 (2014).
8. G. Moula, T. Matsumoto, M. E. Miehlich, K. Meyer, K. Tatsumi, Synthesis of an all-ferric cuboidal iron-sulfur cluster $[Fe^{III}_4S_4(SAr)_4]$. *Angew. Chem. Int. Ed. Engl.* **57**, 11594–11597 (2018).
9. C. J. Pickett, A simple hydrocarbon electrolyte: Completing the electron-transfer series $[Fe_4S_4(SPh)_4]^{1-/2-/3-/4-}$. *J. Chem. Soc. Chem. Commun.* 6, 323–326 (1985).
10. B. V. DePamphilis, B. A. Averill, T. Herskovitz, L. Que Jr., R. H. Holm, Synthetic analogs of the active sites of iron-sulfur proteins. VI. Spectral and redox characteristics of the tetranuclear clusters $[Fe_4S_4(SR)_4]^{2-}$. *J. Am. Chem. Soc.* **96**, 4159–4167 (1974).
11. E. J. Laskowski *et al.*, Synthetic analogues of the 4-Fe active sites of reduced ferredoxins. Electronic properties of the tetranuclear trianions $[Fe_4S_4(SR)_4]^{3-}$ and the structure of $[(C_2H_5)_3(CH_3)N]_3$ [Fe4S4(SC6H5)4]. *J. Am. Chem. Soc.* **100**, 5322–5337 (1978).
12. G. D. Watt, K. R. N. Reddy, Formation of an all ferrous Fe_4S_4 cluster in the iron protein component of *Azotobacter vinelandii* nitrogenase. *J. Inorg. Biochem.* **53**, 281–294 (1994).
13. H. C. Angove, S. J. Yoo, B. K. Burgess, E. Münck, Mössbauer and EPR evidence for an all-ferrous Fe_4S_4 cluster with S=4 in the Fe protein of nitrogenase. *J. Am. Chem. Soc.* **119**, 8730–8731 (1997).
14. H. C. Angove, S. J. Yoo, E. Münck, B. K. Burgess, An all-ferrous state of the Fe protein of nitrogenase. Interaction with nucleotides and electron transfer to the MoFe protein. *J. Biol. Chem.* **273**, 26330–26337 (1998).
15. T. J. Lowery *et al.*, Flavodoxin hydroquinone reduces *Azotobacter vinelandii* Fe protein to the all-ferrous redox state with a $S = 0$ spin state. *Proc. Natl. Acad. Sci. U.S.A.* **103**, 17131–17136 (2006).
16. J. B. Solomon *et al.*, Probing the all-ferrous states of methanogen nitrogenase iron proteins. *JACS Au* **1**, 119–123 (2020).
17. S. Burén, E. Jiménez-Vicente, C. Echavarri-Erasun, L. M. Rubio, Biosynthesis of nitrogenase cofactors. *Chem. Rev.* **120**, 4921–4968 (2020).
18. K. Rupnik *et al.*, Nonenzymatic synthesis of the P-cluster in the nitrogenase MoFe protein: Evidence of the involvement of all-ferrous $[Fe_4S_4]^0$ intermediates. *Biochemistry* **53**, 1108–1116 (2014).
19. C. Goh, B. M. Segal, J. Huang, J. R. Long, R. H. Holm, Polycubane clusters: Synthesis of $[Fe_4S_4(PR_3)_4]^{1+,0}$ (R =But,Cy,Pri) and $[Fe_4S_4]^0$ core aggregation upon loss of phosphine. *J. Am. Chem. Soc.* **118**, 11844–11853 (1996).
20. T. A. Scott, C. P. Berlinguette, R. H. Holm, H. C. Zhou, Initial synthesis and structure of an all-ferrous analogue of the fully reduced $[Fe_4S_4]^0$ cluster of the nitrogenase iron protein. *Proc. Natl. Acad. Sci. U.S.A.* **102**, 9741–9744 (2005).
21. M. Chakrabarti, L. Deng, R. H. Holm, E. Münck, E. L. Bominaar, Mössbauer, electron paramagnetic resonance, and theoretical studies of a carbene-based all-ferrous Fe_4S_4 cluster: Electronic origin and structural identification of the unique spectroscopic site. *Inorg. Chem.* **48**, 2735–2747 (2009).
22. L. Deng, R. H. Holm, Stabilization of fully reduced iron-sulfur clusters by carbene ligation: The $[Fe_nS_n]^0$ oxidation levels (n = 4, 8). *J. Am. Chem. Soc.* **130**, 9878–9886 (2008).
23. E. Münck, E. L. Bominaar, Chemistry. Bringing stability to highly reduced iron-sulfur clusters. *Science* **321**, 1452–1453 (2008).
24. X. Hu, I. Castro-Rodriguez, K. Olsen, K. Meyer, Group 11 metal complexes of N-heterocyclic carbene ligands: nature of the metal carbene bond. *Organometallics* **23**, 755–764 (2004).
25. B. B. Wenke, T. Spatzal, D. C. Rees, Site-specific oxidation state assignments of the iron atoms in the $[4Fe:4S]^{2+/1+/0}$ states of the nitrogenase Fe-protein. *Angew. Chem. Int. Ed. Engl.* **58**, 3894–3897 (2019).
26. P. Strop *et al.*, Crystal structure of the all-ferrous $[4Fe\text{-}4S]^0$ form of the nitrogenase iron protein from *Azotobacter vinelandii*. *Biochemistry* **40**, 651–656 (2001).
27. A. Dey *et al.*, Solvent tuning of electrochemical potentials in the active sites of HiPIP versus ferredoxin. *Science* **318**, 1464–1468 (2007).
28. M. Niemeyer, P. P. Power, Donor-free alkali metal thiolates: Synthesis and structure of dimeric, trimeric, and tetrameric complexes with sterically encumbered terphenyl substituents. *Inorg. Chem.* **35**, 7264–7272 (1996).

29. B. D. Rekken, T. M. Brown, M. M. Olmstead, J. C. Fettinger, P. P. Power, Stable plumbylene dichalcogenolate monomers with large differences in their interligand angles and the synthesis and characterization of a monothiolato Pb(II) bromide and lithium trithiolato plumbate. *Inorg. Chem.* **52**, 3054–3062 (2013).
30. F. Aydin *et al.*, Similarities and differences between potassium and ammonium ions in liquid water: A first-principles study. *Phys. Chem. Chem. Phys.* **22**, 2540–2548 (2020).
31. T. Herskovitz *et al.*, Structure and properties of a synthetic analogue of bacterial iron–sulfur proteins. *Proc. Natl. Acad. Sci. U.S.A.* **69**, 2437–2441 (1972).
32. B. A. Averill, T. Herskovitz, R. H. Holm, J. A. Ibers, Synthetic analogs of the active sites of iron-sulfur proteins. II. Synthesis and structure of the tetra(mercapto-m 3-sulfido-iron) clusters, (Fe 4 S 4 (SR) 4) 2-. *J. Am. Chem. Soc.* **95**, 3523–3534 (1973).
33. Y. Ohki, Y. Ikagawa, K. Tatsumi, Synthesis of new [8Fe-7S] clusters: A topological link between the core structures of P-cluster, FeMo-co, and FeFe-co of nitrogenases. *J. Am. Chem. Soc.* **129**, 10457–10465 (2007).
34. K. Tanifuji *et al.*, A convenient route to synthetic analogues of the oxidized form of high-potential iron-sulfur proteins. *Inorg. Chem.* **53**, 4000–4009 (2014).
35. P. Comba, Coordination compounds in the entatic state. *Coord. Chem. Rev.* **200–202**, 217–245 (2000).
36. M. M. Georgiadis *et al.*, Crystallographic structure of the nitrogenase iron protein from *Azotobacter vinelandii*. *Science* **257**, 1653–1659 (1992).
37. J. L. Schlessman, D. Woo, L. Joshua-Tor, J. B. Howard, D. C. Rees, Conformational variability in structures of the nitrogenase iron proteins from *Azotobacter vinelandii* and *Clostridium pasteurianum*. *J. Mol. Biol.* **280**, 669–685 (1998).
38. F. A. Tezcan *et al.*, Nitrogenase complexes: Multiple docking sites for a nucleotide switch protein. *Science* **309**, 1377–1380 (2005).
39. R. W. F. Hardy, E. Knight, Reductant-dependent adenosine triphosphatase of nitrogen-fixing extracts of *Azotobacter vinelandii*. *Biochim. Biophys. Acta* **122**, 520–531 (1966).
40. M. J. Carney, G. C. Papaefthymiou, K. Spartalian, R. B. Frankel, R. H. Holm, Ground spin state variability in $[Fe_4S_4(SR)_4]^{3-}$. Synthetic analogs of the reduced clusters in ferredoxins and other iron-sulfur proteins: Cases of extreme sensitivity of electronic state and structure to extrinsic factors. *J. Am. Chem. Soc.* **110**, 6084–6095 (1988).
41. P. A. Lindahl, E. P. Day, T. A. Kent, W. H. Orme-Johnson, E. Münck, Mössbauer, EPR, and magnetization studies of the *Azotobacter vinelandii* Fe protein. Evidence for a $[4Fe\text{-}4S]^{1+}$ cluster with spin S = 3/2. *J. Biol. Chem.* **260**, 11160–11173 (1985).
42. M. Hans, W. Buckel, E. Bill, Spectroscopic evidence for an all-ferrous $[4Fe\text{-}4S]^0$ cluster in the superreduced activator of 2-hydroxyglutaryl-CoA dehydratase from *Acidaminococcus fermentans*. *J. Biol. Inorg. Chem.* **13**, 563–574 (2008).
43. T. O'Sullivan, M. M. Millar, Synthesis and study of an analogue for the $[Fe_4S_4]^{3+}$ center of oxidized high-potential iron-sulfur proteins. *J. Am. Chem. Soc.* **107**, 4096–4097 (1985).
44. M. Stelter *et al.*, Structure at 1.0 A resolution of a high-potential iron-sulfur protein involved in the aerobic respiratory chain of *Rhodothermus marinus*. *J. Biol. Inorg. Chem.* **15**, 303–313 (2010).
45. V. Papaefthymiou, M. M. Millar, E. Muenck, Moessbauer and EPR studies of a synthetic analog for the iron-sulfur Fe_4S_4 core of oxidized and reduced high-potential iron proteins. *Inorg. Chem.* **25**, 3010–3014 (1986).
46. Y. Guo, J. Li, "Bioinorganic spectroscopy of iron sulfur proteins–An overview" in *Iron-Sulfur Clusters in Chemistry and Biology*, T. Rouault, Ed. (De Gruyter, 2017), **vol. 1**, chap. 4, pp. 77–134.
47. C. Nave, Radiation damage in protein crystallography. *Radiat. Phys. Chem.* **45**, 483–490 (1995).
48. S. J. Yoo, H. C. Angove, B. K. Burgess, M. P. Hendrich, E. Münck, Mossbauer and integer-spin EPR studies and spin-coupling analysis of the $[4Fe\text{-}4S]^0$ cluster of the Fe protein from *Azotobacter vinelandii* nitrogenase. *J. Am. Chem. Soc.* **121**, 2534–2545 (1999).
49. R. A. Torres, T. Lovell, L. Noodleman, D. A. Case, Density functional and reduction potential calculations of Fe_4S_4 clusters. *J. Am. Chem. Soc.* **125**, 1923–1936 (2003).
50. D. Mitra *et al.*, Characterization of [4Fe-4S] cluster vibrations and structure in nitrogenase Fe protein at three oxidation levels via combined NRVS, EXAFS, and DFT analyses. *J. Am. Chem. Soc.* **135**, 2530–2543 (2013).
51. Y. Ohki *et al.*, Synthetic analogues of $[Fe_4S_4(Cys)_3(His)]$ in hydrogenases and $[Fe_4S_4(Cys)_4]$ in HiPIP derived from all-ferric $[Fe_4S_4\{N(SiMe_3)_2\}_4]$. *Proc. Natl. Acad. Sci. U.S.A.* **108**, 12635–12640 (2011).